

Optical Stokes flow estimation: an imaging-based control approach

Paul Ruhnau · Christoph Schnörr

Received: 14 December 2005 / Revised: 22 August 2006 / Accepted: 6 September 2006 / Published online: 23 November 2006
© Springer-Verlag 2006

Abstract We present an approach to particle image velocimetry based on optical flow estimation subject to physical constraints. Admissible flow fields are restricted to vector fields satisfying the Stokes equation. The latter equation includes control variables that allow to control the optical flow so as to fit to the apparent velocities of particles in a given image pair. We show that when the real unknown flow observed through image measurements conforms to the physical assumption underlying the Stokes equation, the control variables allow for a physical interpretation in terms of pressure distribution and forces acting on the fluid. Although this physical interpretation is lost if the assumptions do not hold, our approach still allows for reliably estimating more general and highly non-rigid flows from image pairs and is able to outperform cross-correlation based techniques.

1 Introduction

1.1 Motivation and overview

Recently, a novel class of variational approaches to image fluid analysis has been introduced in Ruhnau

et al. (2005a, b), Kohlberger et al. (2003). These methods are based on approaches originally developed in the field of computer vision (Horn and Schunck 1981; Nagel and Enkelmann 1986; Schnörr 1991) and suitably elaborated and modified for the purpose of PIV. The prototypical approach presented in Ruhnau et al. (2005) was most recently improved in Corpetti et al. (2005) by taking into account higher-order regularization. For recent improvements concerning correlation-based PIV techniques, we refer to Nobach and Tropea (2005), Nobach et al. (2005) and references therein.

The basic idea of variational optical flow approaches is not to estimate displacement vectors locally and individually, but to estimate vector fields as a whole by minimizing a suitable functional defined over the entire image section. Besides yielding dense flows with a high spatial resolution, a key advantage of these methods is that they allow for the robust estimation of coherent flows by including variational penalty terms that enforce spatial or temporal smoothness of the minimizing vector fields.

In this work, we study a novel optical flow-based approach to *particle image velocimetry* (PIV) that incorporates physical prior knowledge in a more precise and explicit way: all admissible flows for estimation have to satisfy the Stokes equation. In order to estimate the specific flow of apparent velocities of particles in an image sequence, control variables are included and determined by minimizing a suitable objective function which relates the flow and the control variables to given image sequence data. We show that our approach not only estimates the flow from a given PIV image sequence, but pressure and forces acting on the real fluid as well, provided the real flow

P. Ruhnau · C. Schnörr (✉)
Computer Vision, Graphics, and Pattern Recognition
Group, Department of Mathematics and Computer Science,
University of Mannheim, 68131 Mannheim, Germany
e-mail: schnoerr@uni-mannheim.de
URL: <http://www.cvgpr.uni-mannheim.de>

P. Ruhnau
e-mail: ruhnau@uni-mannheim.de

satisfies the Stokes equation, too. Furthermore, numerical experiments presented in this paper in comparison with alternative approaches reveal that fluid flow can also be accurately estimated from image data in more general situations.

We wish to point out that advanced measurement techniques are on the cusp of producing fully time-resolved 3D flow measurements (Elsinga et al. 2005). We expect that this trend will change the current paradigm underlying the algorithm design for flow estimation from image measurements. While 2D-specific problems like out-of-plane motions of particles will become obsolete, the use of physical knowledge in a mathematically and numerically sound way will become natural and important for further progress. Our approach presented in this paper may also be viewed as a first step along this direction.

1.2 Related work

Our approach draws on the general literature on the control of distributed parameter systems (Lions 1971). For specific approaches in connection with fluid dynamics, we refer to Gunzburger (2002). The application of flow control techniques to image motion estimation, as presented in this paper, is novel, however.

Concerning the incorporation of physical constraints for flow estimation through image processing, several interesting approaches have been suggested in the past. Combining PIV and CFD by using cost functions were proposed in Kaga et al. (1998), Ogawara et al. (1997). In contrast to our approach, they can be understood as *post-processing* methods: By correcting cross-correlation velocity estimates so that they approximately conform to the incompressible Navier–Stokes equation, outliers are detected and rectified.

More recently, physics-based non-linear dynamic models (Okuno et al. 2000) have been introduced to PIV. The velocity is again obtained by minimizing a measure which consists of the residues of the Navier–Stokes equation, the continuity equation, and the difference between estimated and observed image data. The resulting non-linear optimization system is solved using methods from evolutionary programming (Michaewicz 1994). This procedure is repeated until the difference between the observed and the estimated image is sufficiently small. In principle, this method allows a reliable estimation of velocity fields and pressure estimates. The need to use general-purpose evolutionary programming indicates, however, that only little insight into the structure of the problem has been gained (existence, multiplicity and stability of

solutions, and related dedicated algorithms). This sharply contrasts with our approach developed below.

The reader may ask: why do we confine ourselves to Stokes flows, as opposed to flows governed by the full Navier–Stokes equation? In this connection, we wish to point out that we consider, for the first time to our knowledge, a quite difficult *inverse problem*—the joint estimation of a flow along with related physical quantities from image sequences. This problem is intricate through the *interaction* of various components, although each of them individually behaves in a mathematically simple way. Therefore, to study the computational feasibility and robustness, we have chosen Stokes flows as a first step which will also be involved as a subroutine through linearization in future extensions of our work. Notwithstanding this restriction, we demonstrated below that our numerical results are competitive with respect to alternative approaches of current research.

1.3 Organization

In Sect. 2 we will present our control approach and the resulting constrained minimization problem. We will detail the finite element discretization, the numerics and features of our coarse-to-fine implementation in Sects. 3.1 and 3.2. A range of numerical experiments on ground-truth image pairs as well as on real-world image sequences will be presented and discussed in Sect. 4. This part is subdivided into experiments that conform with our model and experiments that deviate from it. We conclude in Sect. 5 and indicate extensions within the variational control framework.

2 Approach

2.1 Constrained variational optical flow estimation

Let $I(x, y, t)$ denote the gray value recorded at location $(x, y)^T$ and time t in the image plane. A basic assumption underlying most approaches to motion estimation is that I is conserved, that is the change of $I(x, y, \cdot)$ at location $(x, y)^T$ is due to a movement of $I(x, y, t)$ to the location $(x + u \Delta t, y + v \Delta t)^T$ during a time interval Δt :

$$I(x + u\Delta t, y + v\Delta t, t + \Delta t) \approx I(x, y, t). \quad (1)$$

Here, $\mathbf{u} = (u, v)^T$ denotes the *optical flow*, that is the apparent instantaneous velocity of image structures. The frame rate Δt is assumed to be small, so that $\mathbf{u} \Delta t$ is close to the actual displacement. In the following, we put $\Delta t = 1$ without loss of generality.

A common approach to estimating the *optical flow vector* $(u, v)^T$ at some fixed location $(\bar{x}, \bar{y})^T$ on the image grid $(x, y)^T = (k\Delta x, l\Delta y)^T, k, l \in \mathbb{Z}$, is to assume u and v to be constant within a local spatial area $N(\bar{x}, \bar{y})$ around $(\bar{x}, \bar{y})^T$ and to minimize¹

$$\sum_{k,l \in N(\bar{x}, \bar{y})} [I(k + u\Delta t, l + v\Delta t, t + \Delta t) - I(k, l, t)]^2 \tag{2}$$

as a function of u and v . Assuming additionally that $\sum_{k,l \in N(\bar{x}, \bar{y})} I(k, l, t)^2$ does not vary with $(\bar{x}, \bar{y})^T$, the minimizing values of u, v maximize the correlation function

$$\sum_{k,l \in N(\bar{x}, \bar{y})} I(k + u\Delta t, l + v\Delta t, t + \Delta t) I(k, l, t).$$

Variational motion estimation approaches explicitly take into account smooth changes of the flow $(u, v)^T$ at time t as a function of x and y : $u = u(x, y), v = v(x, y)$. A continuously formulated expression analogous to Eq. 2 then reads:

$$\int_{\Omega} [I(x + u(x, y), y + v(x, y), t + 1) - I(x, y, t)]^2 dx dy. \tag{3}$$

From the viewpoint of variational analysis and algorithm design, formulation (3) is not convenient, however, because the dependency on u and v is non-convex. A common way around this difficulty is (i) to further approximate the objective function so as to obtain a mathematically tractable problem, and (ii) to apply the resulting variational approach to a multi-scale representation of the image data I . Point (i) is addressed by a Taylor series linearization of (3) and by dropping the argument (x, y, t) for convenience:

$$\int_{\Omega} [\nabla I \cdot \mathbf{u} + \partial_t I]^2 dx dy. \tag{4}$$

The spatial and temporal derivatives of I can be estimated locally using FIR filters. Point (ii) above is briefly sketched in Sect. 3.2. For a more detailed account, we refer to Ruhnau et al. (2005).

Problem (4) is not well-posed because *any* vector field with components $\nabla I \cdot \mathbf{u} = -\partial_t I, \forall x, y$, is a minimizer. The standard approach is to add a variational term enforcing smoothness of the flow (Horn and Schunck 1981)

$$\int_{\Omega} \{ (\nabla I \cdot \mathbf{u} + \partial_t I)^2 + \alpha(|\nabla u|^2 + |\nabla v|^2) \} dx dy \tag{5}$$

or smoothness of its divergence and vorticity (Suter 1994)

$$\int_{\Omega} \{ (\nabla I \cdot \mathbf{u} + \partial_t I)^2 + \alpha|\nabla(\nabla \cdot \mathbf{u})|^2 + \beta|\nabla(\text{curl} \mathbf{u})|^2 \} dx dy. \tag{6}$$

In this paper, we investigate an alternative method. Rather than penalizing the estimated flow with a smoothness term, we require as an additional constraint that (4) should be minimized subject to the time-independent² Stokes system describing the steady motion of viscous media:

$$\begin{cases} -\mu\Delta \mathbf{u} + \nabla p = \mathbf{f} & \text{in } \Omega, \\ \nabla \cdot \mathbf{u} = 0 & \text{in } \Omega, \\ \mathbf{u} = \mathbf{g} & \text{on } \Gamma. \end{cases} \tag{7}$$

Here, p denotes the pressure, μ the dynamic viscosity, \mathbf{f} the body force acting on the fluid, and \mathbf{g} the boundary values that are defined on Γ which denotes the boundary of Ω .

Our objective is to determine a body force \mathbf{f} and boundary values \mathbf{g} that yield a velocity field \mathbf{u} which matches the apparent motion (measured by Eq. 4) as well as possible. Note, however, that the minimization of (4) subject to (7) only enforces vanishing divergence of the flow \mathbf{u} . The diffusion term in Eq. 7 has no impact because \mathbf{f} and \mathbf{g} can be chosen so that *every* divergence-free velocity field satisfies the Stokes equation. Therefore, we additionally regularize \mathbf{f} and \mathbf{g} , rendering the whole system mathematically well-posed. As a result, we finally obtain the objective functional

$$\begin{aligned} J(\mathbf{u}, p, \mathbf{f}, \mathbf{g}) = & \int_{\Omega} \frac{1}{2} [\nabla I \cdot \mathbf{u} + \partial_t I]^2 dx \\ & + \int_{\Omega, \Omega_0} \frac{\alpha}{2} |\mathbf{f}|^2 dx + \int_{\Gamma} \frac{\gamma}{2} |\nabla_{\Gamma} \mathbf{g}|^2 d\Gamma \end{aligned} \tag{8}$$

(with $\mathbf{x} = (x, y)^T$) which is to be minimized subject to Eq. 7. Ω_0 in the second term in Eq. 8 denotes regions in the image where we expect large forces acting on the fluid (e.g., interfaces with solids). Therefore, we

¹ Without loss of generality we take $\Delta x = \Delta y = 1$.

² Note that we confine ourselves to the time-independent case as we want to analyze image pairs only and therefore have no additional information about the temporal evolution of the velocity.

exclude body force penalization at these locations. $\nabla_{\Gamma} \mathbf{g}$ denotes the derivative of \mathbf{g} tangential to the boundary.

In terms of control theory (e.g., Gunzburger 2002), the approach can be summarized as follows: we wish to find an optimal state (\mathbf{u}, p) and optimal distributed controls (\mathbf{f}, \mathbf{g}) such that functional J (Eq. 8) is minimized subject to $\mathbf{u}, p, \mathbf{f}$ and \mathbf{g} satisfying the Stokes system (7).

2.2 Optimality conditions

To derive the *optimality system* for determining optimal solutions to Eqs. 8, 7, we transform the constrained optimization problem into an unconstrained optimization with the Lagrangian function

$$L(\mathbf{u}, p, \mathbf{f}, \mathbf{g}, \mathbf{w}, r, \xi) = J(\mathbf{u}, p, \mathbf{f}, \mathbf{g}) \quad (9a)$$

$$- \int_{\Omega} \mathbf{w}^T (-\mu \Delta \mathbf{u} + \nabla p - \mathbf{f}) + r(\nabla \cdot \mathbf{u}) \, dx \quad (9b)$$

$$- \int_{\Gamma} \xi^T (\mathbf{u} - \mathbf{g}) \, d\Gamma \quad (9c)$$

and corresponding multipliers \mathbf{w}, r, ξ . The first-order necessary conditions then yield the optimality system, which determines optimal states and controls:

$$\begin{cases} -\mu \Delta \mathbf{u} + \nabla p = \mathbf{f} & \text{in } \Omega, \\ \nabla \cdot \mathbf{u} = 0 & \text{in } \Omega, \\ \mathbf{u} = \mathbf{g} & \text{on } \Gamma, \end{cases} \quad (10a)$$

$$\begin{cases} \mu \Delta \mathbf{w} + \nabla r = -(\nabla I^T \mathbf{u} + \partial_t I) \nabla I & \text{in } \Omega, \\ \nabla \cdot \mathbf{w} = 0 & \text{in } \Omega, \\ \mathbf{w} = 0 & \text{on } \Gamma, \end{cases} \quad (10b)$$

$$\begin{cases} \mathbf{w} + \alpha \mathbf{f} = 0 & \text{in } \Omega \setminus \Omega_0, \\ \mathbf{w} = 0 & \text{in } \Omega_0, \\ r \mathbf{n} - \mu \frac{\partial \mathbf{w}}{\partial \mathbf{n}} - \gamma \Delta_{\Gamma} \mathbf{g} = 0 & \text{on } \Gamma, \end{cases} \quad (10c)$$

where $\Delta_{\Gamma} \mathbf{g}$ is the 1D Laplacian of \mathbf{g} tangential to the boundary. The *state equation* (10a) results from taking the Gâteaux derivative of (9a, 9b, 9c) in the direction of the Lagrange multipliers, reproducing the Stokes equation (7). Equation 10b is the *adjoint equation*. It specifies the first-order necessary conditions with respect to the state variables \mathbf{u} and p . Note that this equation has the same structure as (10a) with just the variables replaced by the adjoint velocity \mathbf{w} and the adjoint pressure r . Consequently, we can use the same

numerical algorithm to solve (10a) and (10b). The third system of equations (10c) states the *optimality condition*, which is the necessary condition that the gradient of the objective functional with respect to the controls vanishes at the optimum.

We derive next the optimization algorithm for solving (10a, 10b, 10c). Discretization and numerical solution of subproblems (10a) and (10b) are detailed in Sect. 3.1.

2.3 Optimization algorithm

Due to the large number of unknowns in the optimality system (10a, 10b, 10c), we decouple the state system (10a) and the adjoint system (10b), and apply the *gradient method* for computing the solution of the optimal control problem. We therefore first compute the gradients of our objective functional with respect to the body force \mathbf{f} and with respect to the boundary values \mathbf{g} , taking into account the dependency of the state variables on the controls.

When we change the distributed control \mathbf{f} to $\mathbf{f} + \varepsilon \tilde{\mathbf{f}}$, where $\tilde{\mathbf{f}}$ is arbitrary, this change in \mathbf{f} induces the state to change from (\mathbf{u}, p) to $(\mathbf{u} + \varepsilon \mathbf{u}_{\mathbf{f}}, p + \varepsilon p_{\mathbf{f}})$. The change $\mathbf{u}_{\mathbf{f}}$ in the state is determined by the state system, i.e., we have that

$$\begin{cases} -\mu \Delta (\mathbf{u} + \varepsilon \mathbf{u}_{\mathbf{f}}) + \nabla (p + \varepsilon p_{\mathbf{f}}) = \mathbf{f} + \varepsilon \tilde{\mathbf{f}} \\ \nabla \cdot (\mathbf{u} + \varepsilon \mathbf{u}_{\mathbf{f}}) = 0 \\ (\mathbf{u} + \varepsilon \mathbf{u}_{\mathbf{f}}) = \mathbf{g} \end{cases} \quad \text{on } \Gamma. \quad (11)$$

For $\varepsilon \rightarrow 0$ this leads to the so-called sensitivity equation

$$\begin{cases} -\mu \Delta \mathbf{u}_{\mathbf{f}} + \nabla p_{\mathbf{f}} = \tilde{\mathbf{f}} \\ \nabla \cdot \mathbf{u}_{\mathbf{f}} = 0 \\ \mathbf{u}_{\mathbf{f}} = 0 \end{cases} \quad \text{on } \Gamma. \quad (12)$$

This equation means that an infinitesimal change of the control function \mathbf{f} in the “direction” of $\tilde{\mathbf{f}}$ induces the infinitesimal change in the “direction” of $\mathbf{u}_{\mathbf{f}}$ and $p_{\mathbf{f}}$. Next, let us derive a formula for the change in the functional $J(\mathbf{u}, \mathbf{f})$ of Eq. 8 effected by an infinitesimal change in the direction $\tilde{\mathbf{f}}$ in the control \mathbf{f} . We will keep track of both the explicit dependence of J on \mathbf{f} and the implicit dependence through the state (\mathbf{u}, p) :

$$\begin{aligned} \langle \partial_{\mathbf{f}} J, \tilde{\mathbf{f}} \rangle &= \left. \frac{\partial J(\mathbf{u} + \varepsilon \mathbf{u}_{\mathbf{f}}, p + \varepsilon p_{\mathbf{f}}, \mathbf{f} + \varepsilon \tilde{\mathbf{f}})}{\partial \varepsilon} \right|_{\varepsilon=0} \\ &= \int_{\Omega} \left\{ (\nabla I^T \mathbf{u} + I_t) \nabla I^T \mathbf{u}_{\mathbf{f}} + \alpha \mathbf{f}^T \tilde{\mathbf{f}} \right\} \, dx. \end{aligned} \quad (13)$$

Substitution of the first adjoint equation (10b) yields

$$\langle \partial_{\mathbf{f}} J, \tilde{\mathbf{f}} \rangle = \int_{\Omega} \left\{ -(\mu \Delta \mathbf{w} + \nabla r)^T \mathbf{u}_{\mathbf{f}} + \alpha \mathbf{f}^T \tilde{\mathbf{f}} \right\} d\mathbf{x}. \tag{14}$$

Integrating by parts yields

$$\begin{aligned} \langle \partial_{\mathbf{f}} J, \tilde{\mathbf{f}} \rangle &= \int_{\Omega} \left\{ -\mu \Delta \mathbf{u}_{\mathbf{f}}^T \mathbf{w} + \nabla \cdot \mathbf{u}_{\mathbf{f}} r + \alpha \mathbf{f}^T \tilde{\mathbf{f}} \right\} d\mathbf{x} \\ &\quad + \int_{\Gamma} \left\{ \mu \left(-\mathbf{u}_{\mathbf{f}}^T \frac{\partial \mathbf{w}}{\partial \mathbf{n}} + \mathbf{w}^T \frac{\partial \mathbf{u}_{\mathbf{f}}}{\partial \mathbf{n}} \right) + \mathbf{u}_{\mathbf{f}}^T r \mathbf{n} \right\} d\Gamma. \end{aligned} \tag{15}$$

The boundary integral is zero, as \mathbf{w} and $\mathbf{u}_{\mathbf{f}}$ are zero at the boundaries. Now we can substitute the sensitivity equation (12) into (15)

$$\langle \partial_{\mathbf{f}} J, \tilde{\mathbf{f}} \rangle = \int_{\Omega} \left\{ (\tilde{\mathbf{f}} - \nabla p_{\mathbf{f}})^T \mathbf{w} + \alpha \mathbf{f}^T \tilde{\mathbf{f}} \right\} d\mathbf{x}. \tag{16}$$

Again, integration by parts and substitution of the second adjoint equation finally leads to

$$\langle \partial_{\mathbf{f}} J, \tilde{\mathbf{f}} \rangle = \int_{\Omega} \left\{ \mathbf{w}^T \tilde{\mathbf{f}} + \alpha \mathbf{f}^T \tilde{\mathbf{f}} \right\} d\mathbf{x}. \tag{17}$$

An analogue derivation yields the gradient of J in \mathbf{g} -direction:

$$\langle \partial_{\mathbf{g}} J, \tilde{\mathbf{g}} \rangle = \int_{\Gamma} \left\{ -\mu \left(\frac{\partial \mathbf{w}}{\partial \mathbf{n}} \right)^T \tilde{\mathbf{g}} + r \mathbf{n}^T \tilde{\mathbf{g}} + \gamma \nabla_{\Gamma} \mathbf{g}^T \nabla_{\Gamma} \tilde{\mathbf{g}} \right\} d\Gamma. \tag{18}$$

Now that we have found formulas for the gradients of our objective functional, we can develop the gradient algorithm:

We start with a velocity field $\mathbf{u} = \mathbf{0}$ (or with any other initial value) and solve the adjoint equation. Computing the gradient of the functional with respect to \mathbf{g} and \mathbf{f} , respectively (cf. Eqs. 17 and 18), yields

$$\partial_{\mathbf{f}} J = \mathbf{w} + \alpha \mathbf{f} \tag{19a}$$

$$\begin{aligned} \partial_{\mathbf{g}} J &= r \mathbf{n} - \mu \frac{\partial \mathbf{w}}{\partial \mathbf{n}} - \gamma \Delta_{\Gamma} \mathbf{g} - \frac{\mathbf{n}}{|\Gamma|} \int_{\Gamma} \left(-\mu \frac{\partial \mathbf{w}}{\partial \mathbf{n}} + r \mathbf{n} - \gamma \Delta_{\Gamma} \mathbf{g} \right) \\ &\quad \cdot \mathbf{n} d\Gamma = 0. \end{aligned} \tag{19b}$$

Note that r is determined by the adjoint equation (10b) only up to a constant. Equation 19b chooses this

constant so that the update of \mathbf{g} satisfies the compatibility condition $\int_{\Gamma} \mathbf{g} \cdot \mathbf{n} d\Gamma = 0$ (sum of inflow = sum of outflow must be valid for incompressible fluids). Having updated the controls, we solve the state equation and proceed to the next iteration. After convergence of the algorithm, the iterates satisfy Eq. 10c, too.

Experiments have shown that using two individual and adaptive step sizes for \mathbf{f} and \mathbf{g} , respectively, is computationally both more reliable and efficient. This leads to the algorithm 1 listed below. Note that the stepsize parameters τ_f and τ_g are automatically selected by the algorithm.

Algorithm 1 Gradient Algorithm

- 1: set initial $\mathbf{u} = 0$
 - 2: choose tolerance ε
 - 3: $\tau_f := 1, \tau_g := 1, \mathbf{f}_0 := 0, \mathbf{g}_0 := 0$
 - 4: **repeat**
 - 5: solve (10b) for (\mathbf{w}, r)
 - 6: $\mathbf{f}_i = \mathbf{f}_{i-1} - \tau_f (\alpha \mathbf{f}_{i-1} + \mathbf{w})$
 - 7: solve (10a) for \mathbf{u}
 - 8: **if** $J(\mathbf{u}, \mathbf{f}_i) \leq J(\mathbf{u}, \mathbf{f}_{i-1})$ **then**
 - 9: $\tau_f := \tau_f / 2$
 - 10: GOTO 6
 - 11: **else**
 - 12: $\tau_f := 3/2 \tau_f$
 - 13: **end if**
 - 14: solve (10b) for (\mathbf{w}, r)
 - 15: $\mathbf{g}_i = \mathbf{g}_{i-1} - \tau_g \left[r \mathbf{n} - \mu \frac{\partial \mathbf{w}}{\partial \mathbf{n}} - \gamma \Delta_{\Gamma} \mathbf{g} - \frac{\mathbf{n}}{|\Gamma|} \int_{\Gamma} \left(-\mu \frac{\partial \mathbf{w}}{\partial \mathbf{n}} + r \mathbf{n} - \gamma \Delta_{\Gamma} \mathbf{g} \right) \cdot \mathbf{n} d\Gamma \right]$
 - 16: solve (10a) for \mathbf{u}
 - 17: **if** $J(\mathbf{u}, \mathbf{g}_i) \leq J(\mathbf{u}, \mathbf{g}_{i-1})$ **then**
 - 18: $\tau_g := \tau_g / 2$
 - 19: GOTO 15
 - 20: **else**
 - 21: $\tau_g := 3/2 \tau_g$
 - 22: **end if**
 - 23: **until** $|J(\mathbf{u}, \mathbf{f}_i, \mathbf{g}_i) - J(\mathbf{u}, \mathbf{f}_{i-1}, \mathbf{g}_{i-1})| / |J(\mathbf{u}, \mathbf{f}_i, \mathbf{g}_i)| < \varepsilon$
-

2.4 Relaxing the assumption of vanishing divergence

Due to out-of-plane motion, that cannot be completely avoided in 2D, the assumption of a vanishing divergence will often not hold in practice. Optical Stokes Flow’s strict enforcement of a vanishing divergence may lead to large errors in the velocity field if this assumption is violated.

Let us therefore modify the prior knowledge that we use:

$$\begin{cases} -\mu \Delta \mathbf{u} + \nabla p &= \mathbf{f} & \text{in } \Omega, \\ \nabla \cdot \mathbf{u} &= -\frac{\partial u_3}{\partial z} & \text{in } \Omega, \\ \mathbf{u} &= \mathbf{g} & \text{on } \Gamma. \end{cases} \tag{20}$$

where u_3 is the out-of-plane component (component in z direction). Note, however, that u_3 is unknown and cannot be extracted from the algorithm’s 2D input data. This is why we impose an additional constraint: $d = \frac{\partial u_3}{\partial z}$ should be small. This leads to the overall optimization problem:

$$J(\mathbf{u}, p, \mathbf{f}, \mathbf{g}, d) = \int_{\Omega} \frac{1}{2} [\nabla I \cdot \mathbf{u} + \partial_t I]^2 dx + \int_{\Omega \setminus \Omega_0} \frac{\alpha}{2} |\mathbf{f}|^2 dx + \int_{\Omega} \frac{\beta}{2} |d|^2 dx + \int_{\Gamma} \frac{\gamma}{2} |\nabla_{\Gamma} \mathbf{g}|^2 d\Gamma \tag{21}$$

which is to be minimized subject to Eq. 20. The corresponding optimization algorithm is equivalent to the one presented in Sect. 2.3. The gradient of the additional control d completes (19a, 19b)

$$\partial_d J = \beta d + r. \tag{22}$$

3 Discretization and implementation

3.1 Solving the subproblems

In order to apply algorithm 1 to the optimality system (10a, 10b), we have to solve two saddle point problems corresponding to the state equation (10a) and to the adjoint equation (10b), respectively. In this section, we explain how these problems are discretized and numerically solved.

The unique vector field $\mathbf{u}(x, y)$ solving (Eq. 12) is determined by the variational system

$$\begin{aligned} a(\mathbf{u}, \tilde{\mathbf{u}}) + b(p, \tilde{\mathbf{u}}) &= (\mathbf{f}, \tilde{\mathbf{u}}), \quad \forall \tilde{\mathbf{u}} \\ b(\tilde{p}, \mathbf{u}) &= 0, \quad \forall \tilde{p} \end{aligned} \tag{23}$$

and a similar variational system determines the unique solution \mathbf{w} to Eq. 10b. Accordingly, we define for the Stokes problem and for the adjoint problem, respectively, bilinear forms and linear forms:

$$a_{St}(\mathbf{u}, \tilde{\mathbf{u}}) := \int_{\Omega} \mu \nabla \mathbf{u} \cdot \nabla \tilde{\mathbf{u}} dx \tag{24}$$

$$a_{Adj}(\mathbf{w}, \tilde{\mathbf{w}}) := \int_{\Omega} -\mu \nabla \mathbf{w} \cdot \nabla \tilde{\mathbf{w}} dx$$

$$b_{St}(p, \tilde{\mathbf{u}}) := - \int_{\Omega} p \nabla \cdot \tilde{\mathbf{u}} dx$$

$$b_{Adj}(r, \tilde{\mathbf{w}}) := - \int_{\Omega} r \nabla \cdot \tilde{\mathbf{w}} dx \tag{25}$$

and the right hand sides:

$$(\mathbf{f}_{St}, \tilde{\mathbf{u}}) := \int_{\Omega} \mathbf{f} \cdot \tilde{\mathbf{u}} dx$$

$$(\mathbf{f}_{Adj}, \tilde{\mathbf{w}}) := \int_{\Omega} -(\nabla I^T \mathbf{u} + \partial_t I) \nabla I \cdot \tilde{\mathbf{w}} dx. \tag{26}$$

We choose a regular tessellation of the image domain Ω and discretize (23) using finite elements. It is well-known from computational fluid dynamics that standard first-order finite element discretizations may result in non-physical pressure oscillations or even in so-called locking effects, where the zero velocity field is the only one satisfying the incompressibility condition.

Therefore, when solving the Stokes problem, mixed finite elements are traditionally used. An admissible choice is the so-called Taylor–Hood element based on a square reference element with nine nodes (Fig. 1). Each component of velocity fields is defined in terms of piecewise quadratic basis functions ψ located at each node, whereas pressure fields are represented by linear basis functions ϕ attached to each corner node. It can be shown that Taylor–Hood elements fulfil the so-called Babuska–Brezzi condition (Brezzi and Fortin 1991), that is the

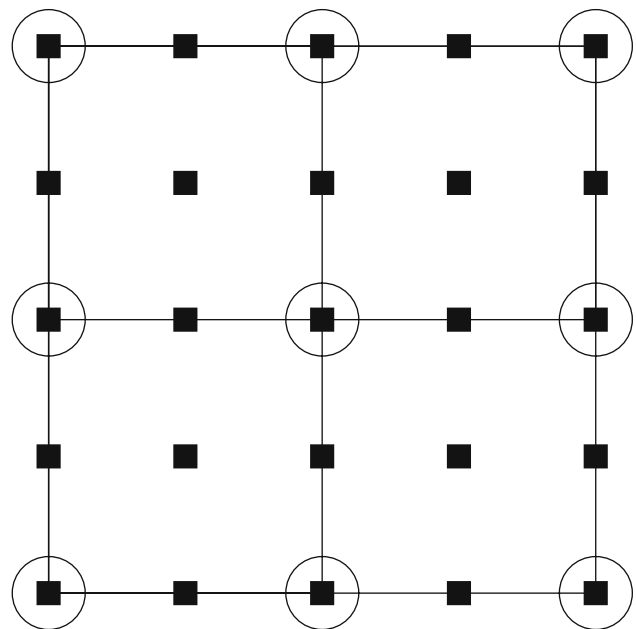


Fig. 1 Sketch of 2D Taylor–Hood elements: biquadratic velocity elements (squares) and bilinear pressure elements (circles)

discretized problem is well-posed and numerically stable. Indexing each velocity node (squares of Fig. 1) by 1, 2, ..., N , we obtain

$$u(x, y) = \sum_{i=1}^N u_i \psi_i(x, y) \tag{27}$$

and similarly for $v(x, y)$ and the components of $\mathbf{w}, \tilde{\mathbf{u}}, \tilde{\mathbf{w}}$. By analogy, we obtain for the M pressure nodes (circles of Figs. 1, 2)

$$p(x, y) = \sum_{i=1}^M p_i \phi_i(x, y) \tag{28}$$

and similarly expressions for $p, r, \tilde{p}, \tilde{r}$. Hence, each function $\mathbf{u}, \mathbf{w}, \tilde{\mathbf{u}}, \tilde{\mathbf{w}}$ is represented by $2N$ real variables, and each function $p, r, \tilde{p}, \tilde{r}$ is represented by M real variables. For the sake of simplicity, we will use the same symbols to denote these vectors. Equation 23 then reads

$$\begin{aligned} \mathbf{A}\mathbf{u} \cdot \tilde{\mathbf{u}} + \mathbf{B}^T p \cdot \tilde{\mathbf{u}} &= \mathbf{f} \cdot \tilde{\mathbf{u}}, \quad \forall \tilde{\mathbf{u}} \\ \mathbf{B}\mathbf{u} \cdot \tilde{p} &= 0, \quad \forall \tilde{p} \end{aligned} \tag{29}$$

Hence, we obtain the discretized Stokes system

$$\begin{aligned} \mathbf{A}\mathbf{u} + \mathbf{B}^T p &= \mathbf{f} \\ \mathbf{B}\mathbf{u} &= 0 \end{aligned} \tag{30}$$

and a similar system for the adjoint equation. The $2N \times 2N$ -matrix \mathbf{A} factorizes into

$$\mathbf{A} = \begin{pmatrix} A_{11} & 0 \\ 0 & A_{22} \end{pmatrix}, \tag{31}$$

where by virtue of (30):

$$\begin{aligned} (A_{11})_{k,l} &= a((\psi_k, 0)^T, (\psi_l, 0)^T), \\ (A_{22})_{k,l} &= a((0, \psi_k)^T, (0, \psi_l)^T). \end{aligned} \tag{32}$$

The $M \times 2N$ -matrix \mathbf{B} factorizes into

$$\mathbf{B} = (\mathbf{B}_1 \quad \mathbf{B}_2), \tag{33}$$

where by virtue of (25)

$$\begin{aligned} (\mathbf{B}_1)_{k,l} &= b(\phi_k, (\psi_l, 0)^T), \\ (\mathbf{B}_2)_{k,l} &= b(\phi_k, (0, \psi_l)^T). \end{aligned} \tag{34}$$

Finally, the $2N$ -vector \mathbf{f} factorizes into $\mathbf{f} = (\mathbf{f}_1^T, \mathbf{f}_2^T)^T$ where by virtue of (26)

$$\begin{aligned} (\mathbf{f}_1)_k &= (\psi_k, 0), \\ (\mathbf{f}_2)_k &= (0, \psi_k). \end{aligned} \tag{35}$$

In order to numerically solve the saddle point problem (30), we employ the Uzawa algorithm (cf. e.g., Braess 1997). Since the matrix \mathbf{A} is positive definite, we solve the first equation of the system (30) for the unknown \mathbf{u} :

$$\mathbf{u} = \mathbf{A}^{-1}(\mathbf{f} - \mathbf{B}^T p) \tag{36}$$

and insert the result in the second equation

$$\mathbf{B}\mathbf{A}^{-1}(\mathbf{f} - \mathbf{B}^T p) = 0. \tag{37}$$

This gives a problem which only incorporates the pressure

$$(\mathbf{B}\mathbf{A}^{-1}\mathbf{B}^T)p = \mathbf{B}\mathbf{A}^{-1}\mathbf{f}. \tag{38}$$

The matrix $(\mathbf{B}\mathbf{A}^{-1}\mathbf{B}^T)$ is symmetric and positive definite. Therefore, we apply the conjugate gradient

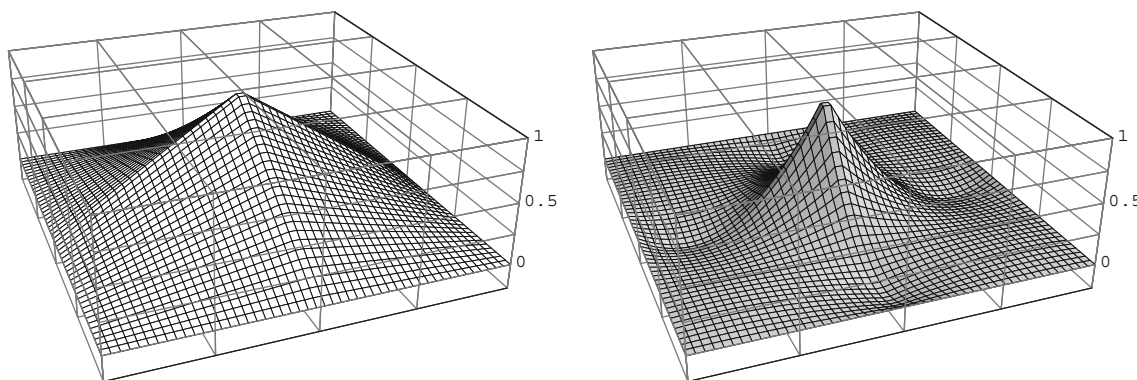


Fig. 2 Left: Basis function ϕ of a bilinear finite element. Right: Basis function ψ of a biquadratic finite element

algorithm to (38). This requires a single matrix inversion in every iteration step. For computational efficiency, this is accomplished using a multigrid iteration (cf. Hackbusch 1993). Note that A is just the system matrix of the Poisson equation. For 2D problems, A can be split into two systems (one for every dimension, cf. Eq. 31), that can be solved in parallel. Algorithm 2 details the overall process.

Algorithm 2 Uzawa Algorithm

- 1: $p_0 \in \mathbb{R}, A\mathbf{u}_1 = \mathbf{f} - B^T p_0$. Set $d_1 = -q_1 = B \mathbf{u}_1$.
 - 2: **repeat**
 - 3: $p_k = B^T d_k$
 - 4: Approx. $h_k = A^{-1} p_k$ using multigrid
 - 5: $\alpha_k = d_k^T d_k / (p_k^T h_k)$
 - 6: $p_k = p_{k-1} - \alpha_k d_k$
 - 7: $\mathbf{u}_{k+1} = \mathbf{u}_k + \alpha_k h_k$
 - 8: $q_{k+1} = -B \mathbf{u}_{k+1}$
 - 9: $\beta_k = q_{k+1}^T q_{k+1} / (q_k^T q_k)$
 - 10: $d_{k+1} = -q_{k+1} + \beta_k d_k$
 - 11: **until** $q_{k+1} < \varepsilon$
-

3.2 Coarse-to-fine approach

Due to the Taylor series linearization inherent in the optical flow constraint, only slow motion can be accurately computed by minimizing (Eq. 4) (approx. up to 1 pixel between exposures). This is why we apply our approach to a multi-scale representation of the image data I : we first compute a coarse motion field by using only low spatial frequency components and undo the motion, thus roughly stabilizing the position of the image over time. Then the higher frequency subbands are used to estimate the optical flow on the warped sequence. Combining this optical flow correction with the previously computed optical flow yields a refined overall optical flow estimate. This process is repeated at finer spatial scales until the original image resolution is reached. For further details about coarse-to-fine optical flow estimation (use of FIR filters, interpolation, ...) we refer the interested reader to Ruhnau et al. (2005).

Let \mathbf{u} denote the overall velocity that results from our computations, \mathbf{u}_{old} the current estimate of this overall velocity, and $\partial_t I_w$ the temporal derivative computed as difference between the second image—warped with \mathbf{u}_{old} —and the first image. Then Eq. 4 can be reformulated as

$$J(\mathbf{u}) = \int_{\Omega} \frac{1}{2} (\nabla I^T (\mathbf{u} - \mathbf{u}_{old}) + \partial_t I_w)^2 dx. \tag{39}$$

Note that motion over the image boundary Γ prevents the computation of the spatial and temporal gradients

of the warped image I_w at specific locations. In order to avoid error-prone filling-in heuristics (that use gradient information from surrounding areas), we simply omit the evaluation of the data term at these particular locations.³ This reformulation does not affect the state system and the optimality condition. The adjoint system, on the other hand, is transformed into

$$\begin{cases} \mu \Delta \mathbf{w} + \nabla r &= -(\nabla I^T (\mathbf{u} - \mathbf{u}_{old}) + \partial_t I_w) \nabla I & \text{in } \Omega, \\ \nabla \cdot \mathbf{w} &= 0 & \text{in } \Omega, \\ \mathbf{w} &= 0 & \text{on } \Gamma. \end{cases} \tag{40}$$

We could now—as we did in algorithm 1—start at every resolution level with an initial zero velocity field. This is a poor initialization, however: we know that \mathbf{u}_{old} is a good approximation of the true velocity field: therefore, we solve Eq. 10a for (\mathbf{u}, p) before the first iteration of every resolution level, using bilinearly interpolated versions of \mathbf{f} and \mathbf{g} from the preceding level. We obtain an initial velocity \mathbf{u} that both satisfies Eq. 10a and is a good approximation of the true velocity field.

4 Experimental evaluation

This experimental section is divided into two main parts:

- In Sect. 4.1 we present synthetic experiments that fulfil the Stokes equation (i.e., creeping flows). Besides the question of the accuracy of our method, we want to go further into the question of how meaningful the asserted estimates for pressure p and body force \mathbf{f} prove to be.
- In Sect. 4.2 we show (for synthetic and real-world image pairs) that one can also achieve good velocity estimates for highly non-rigid flows. In these cases, however, we cannot expect the body-force and the pressure distribution to contain physically relevant information.

4.1 Stokes flows

We have selected two flow scenarios for which analytic solutions exist due to symmetry: *Poiseuille flow* is a viscous flow between two parallel plates and the section *Flow in an Annular Gap* examines the viscous flow between two infinitely long cylinders.

³ Note that due to the regularizer, we will still get reliable velocity estimates at these locations.

4.1.1 Poiseuille flow

We consider an incompressible Newtonian fluid with constant density and viscosity flows between two parallel plates (at $y = 0$ and $y = h$) with infinite width. The x -axis points in the direction of the flow. The velocity distribution for such a system is given by (e.g., Landau and Lifschitz 1952)

$$u(y) = -\frac{1}{2\mu} \frac{\partial p}{\partial x} \left(\frac{h^2}{4} - \left(y - \frac{h}{2} \right)^2 \right). \quad (41)$$

This means that we can expect a parabolic velocity profile, with the largest velocity in the middle between the two plates. For our synthetic experiment, we chose $\mu = 1$, $h = 257$ pixels, and $\frac{\partial p}{\partial x} = -1 \times 10^{-3}$. This choice yields a maximum velocity of 8.256 pixels between two exposures. Figure 3 shows the synthetic image and the target velocity field with which the image was warped in order to get a synthetic image pair. We used the same techniques as described in Okamoto et al. (2000) (10,000 particles, 3 pixels average particle diameter, 1 pixel standard deviation). As the Poiseuille flow is truly 2D, the third component is zero everywhere. Please note that while in numerical hydrodynamics one is accustomed to small mesh sizes ($s \ll 1$) and small volumes ($\text{VOL} \approx 1$), we measure in terms of pixels here. This is why the parameter choice may appear uncommon.

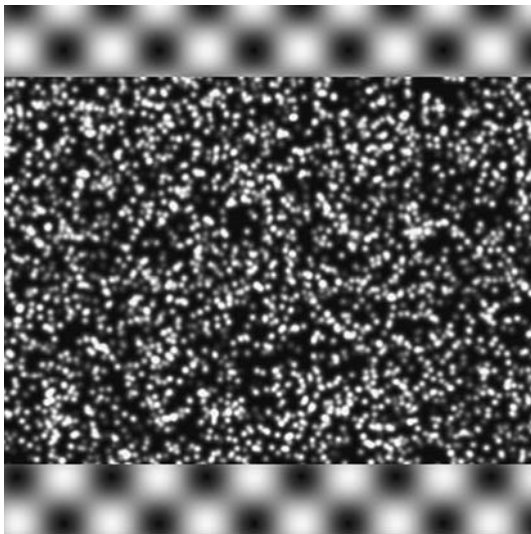


Fig. 3 Poiseuille flow: incompressible Newtonian fluid with constant density and viscosity flows between two parallel plates. This creeping flow satisfies the Stokes equation. *Left:* Synthetic PIV image. *Right:* Target velocity field

In a first experiment, we set $\alpha = 100$ and $\gamma = 200$, and we penalized the body force everywhere (i.e., $\Omega_0 = \emptyset$). Figure 4 shows the reconstructed velocity component u . The estimated velocity is almost exact (cf. also Fig. 6), its RMS error is ≈ 0.0734 pixels. However, Fig. 6 also shows that there are problems at the boundaries of the plates. They are caused by the forces acting on the fluid. In fact, the locations where forces act on the fluid are just boundaries of the plates: The pressure-induced force acts orthogonally to the interfaces and is

$$f_x = -p\mathbf{n}. \quad (42)$$

The frictional force at the interfaces acts in opposite flow direction and is

$$f_y = \frac{h\partial p}{2\partial x}. \quad (43)$$

Figure 4, left, shows that the algorithm has in fact detected a force at the interfaces that acts in opposite flow direction. However, the method also detects a (smaller) force in the middle of the pipe that acts in flow direction. The reason for this error is quite obvious: in Eq. 8, we added constraints on the body force that penalize the L_2 norm of \mathbf{f} . The correct body force, however, has an extremely high L_2 norm at the interfaces. In order to yet compute a reliable body force—and thus also pressure estimates, as the pressure depends on velocity *and* body force—we have to tell the algorithm at what locations forces are likely to act on the fluid. Then we can exclude the body force penalization at these locations.

Accordingly, in a second experiment, we switched off body force penalization at the interfaces of the two parallel plates (at $y = 0$ and $y = h$). The results can be seen in Fig. 5, right: The reconstructed body force is reasonable, the share that acts in reverse flow direction is the frictional force (cf. Eq. 43) and the part that acts orthogonally to the flow direction is the pressure-induced force (cf. Eq. 42).

Figure 6 shows that also the RMS error has decreased considerably ($\text{RMS} \approx 0.0212$ pixels). Note that there are still errors at the ends of the interfaces, the reason for these errors is the regularization of the boundary values g (cf. Eq. 8). The smoothness of the boundary values enforced by Eq. 8 deviates from reality at these locations.

Figure 4 shows the reconstructed pressure field on the right. Taking a closer look at the pressure derivative in flow direction (cf. Fig. 7), we see that the pressure derivative inside the tube is approx. 4×10^{-3} , which is the correct reconstruction. We point out that due to the mixed finite element discretization, the

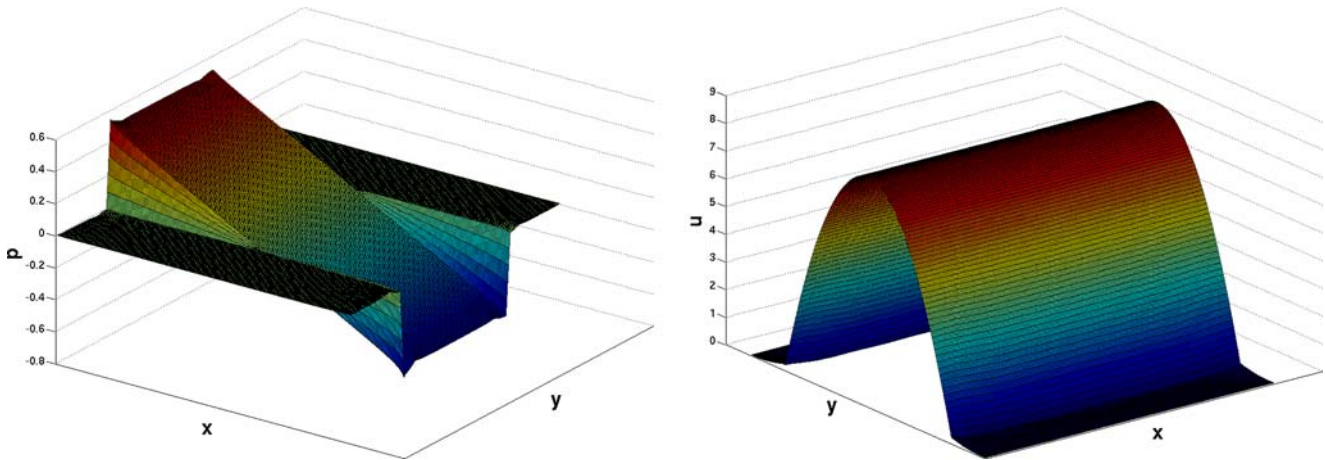


Fig. 4 *Left:* Optical Stokes flow is able to reconstruct the parabolic velocity profile extremely accurately. *Right:* Using fluid-mechanics priors, even the true pressure distribution can be reconstructed. Note the linear pressure decrease in flow direction

Fig. 5 Reconstructed body force. Note that the *arrows* are scaled in order to be visible. If we specify regions at which forces are expected to act on the fluid (i.e., solid–fluid interfaces), even forces that act on the boundary can be reconstructed. *Left:* \mathbf{f} is penalized everywhere (scaling factor: 2,000). *Right:* no penalization of \mathbf{f} at the interfaces (scaling factor: 50)

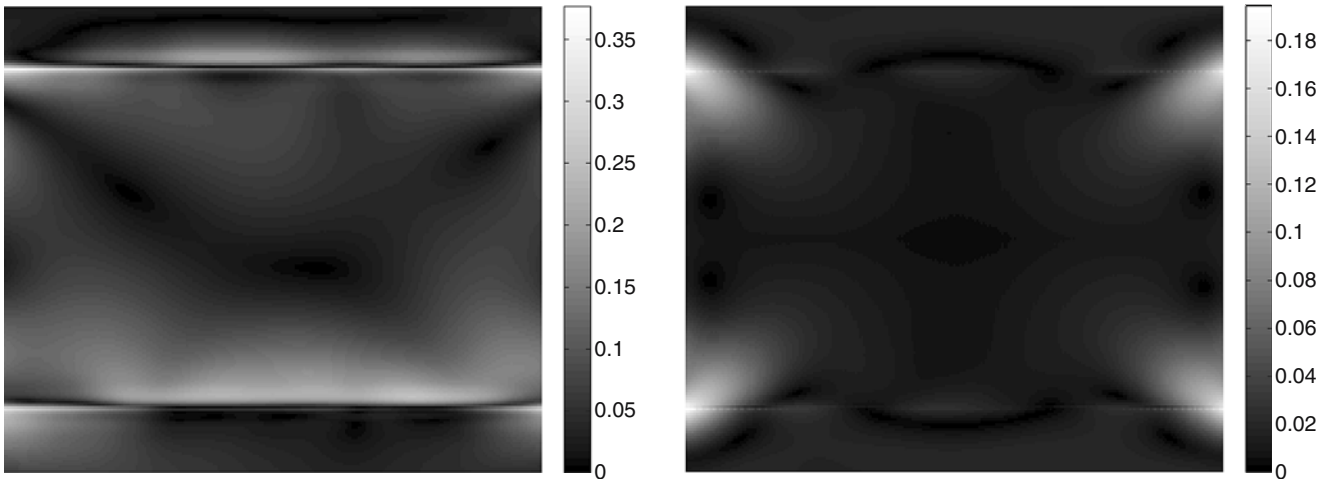
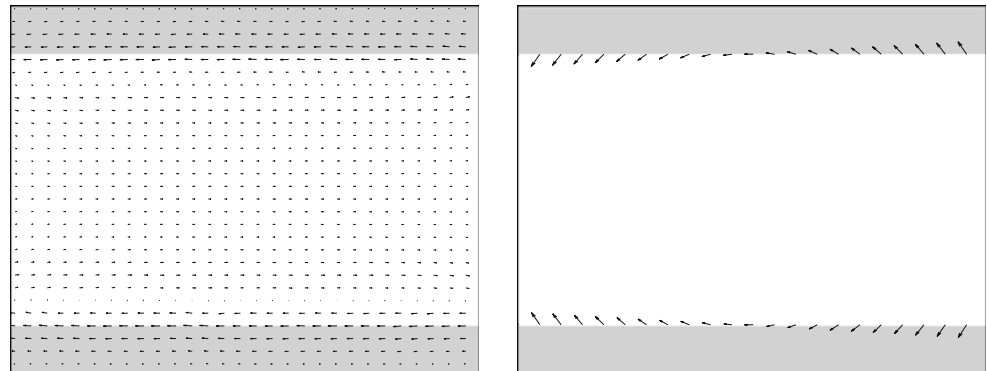


Fig. 6 *Left:* If we penalize \mathbf{f} everywhere, the mean RMS error is 0.0734 pixels. *Right:* By specifying the solid–liquid interfaces, the RMS error decreases to 0.0212 pixels

resolution of the pressure field is smaller than the resolution of the reconstructed velocity. Therefore, the pressure derivative has to be scaled with the factor 4.

4.1.2 Flow in an annular gap

Suppose an incompressible Newtonian fluid flows steadily within the annular gap of two infinitely long

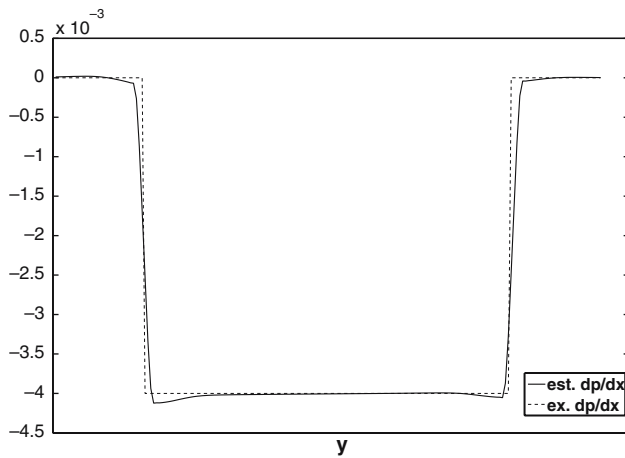


Fig. 7 Profile of the averaged pressure derivative in flow direction. Note that the linear pressure decrease in flow direction (-4×10^{-3} inside the pipe) is recovered extremely accurately

cylinders (R_1, R_2). The outer cylinder is fixed, while the inner cylinder rotates with angular speed Ω . The velocity distribution for such a setting is given by (e.g., Landau and Lifschitz 1952)

$$v(r) = \frac{\Omega R_2^2}{R_2^2 - R_1^2} r + \frac{\Omega R_1^2 R_2^2}{R_2^2 - R_1^2} \frac{1}{r} \tag{44}$$

The pressure is constant.⁴ For our synthetic example, we have chosen $R_1 = 100, R_2 = 220, \Omega = 0.1$ and $\mu = 1$. This leads to a maximum displacement of 10 pixels between two exposures. Figure 8 shows the synthetic image as well as the target velocity field. We set $\alpha = 100, \gamma = 200$ and $\Omega_0 = \emptyset$ in a first experiment.

Figure 9 shows the reconstructed velocity field. The velocity field looks very reasonable. Figure 13, however, shows clearly a large error at the cylinder interfaces, in particular at the interface of the inner cylinder. This error occurs for the same reason as in the preceding example. The acting force is very large and punctiform at the inner cylinder interface. This contradicts the assumptions made in Eq. 8.

We next chose the same approach as in the preceding section to deal with the problem, that is avoiding body force penalization at the boundaries. This leads to very good results. The average RMS error decreases to 0.0079 pixels (cf. Fig. 13). Figure 10, right, shows that the velocity profile agrees exactly with the analytically computed profile. The tangential and orthogonal forces at the two

cylinder interfaces also correspond very well with the analytically computed forces. The forces in tangential direction read:

$$\begin{aligned} f_{R_1} &= -2\mu \frac{\Omega R_2^2}{R_2^2 - R_1^2}, \\ f_{R_2} &= -2\mu \frac{\Omega R_1^2}{R_1^2 - R_2^2}. \end{aligned} \tag{45}$$

The pressure is zero everywhere (cf. Fig. 10, left). There are only minor problems at the cylinder boundaries due to an increased numerical sensitivity. A reason is that we deliberately omitted regularization of f at these locations, for the sake of accurate reconstruction (Figs. 11, 12, 13).

4.1.3 Noise and robustness

To examine the robustness of our reconstruction approach with respect to image noise, we repeated the annular gap experiment (Sect. 4.1.2) but superimposed white noise with a variance up to 50% of the grayvalue range.

Figure 14 shows that the RMS velocity error increases moderately only as a function of noise variance. This result proves a pronounced robustness of our approach. Most remarkable is the observation that the accuracy of the reconstruction appears to be *beyond* what can be extracted from the raw data *without* any physical prior knowledge.

4.2 Navier–Stokes flows

In the forthcoming examples, the assumption of a Stokes flow is definitely not valid, as these turbulent flows are mainly governed by the convection term of the Navier–Stokes equations. Therefore, we cannot expect the pressure or body-force to be physically accurate. However, our approach can also be used for these high Reynolds numbers. The Stokes equation then merely serves as a regularization term, and the body-force can be chosen so as to mimic the nonlinear effects of the convection term.

4.2.1 Synthetic highly non-rigid image pair

We studied a synthetic PIV image pair provided by Carlier and Heitz (2005). The underlying highly non-rigid velocity field was computed by a so-called pseudo-spectral code that solves the vorticity transport equation in Fourier space and evaluates a subgrid model for simulating small-scale turbulent effects on the larger scales of the flow. The synthetic image

⁴ This is only true when solving the problem with the Stokes equation. If we had used the Navier–Stokes equations, the pressure distribution would read $\frac{\partial p}{\partial r} = \frac{\sigma v^2}{r}$.

Fig. 8 Creeping flow between two rotating cylinders. *Left:* Synthetic PIV image. *Right:* Target velocity field

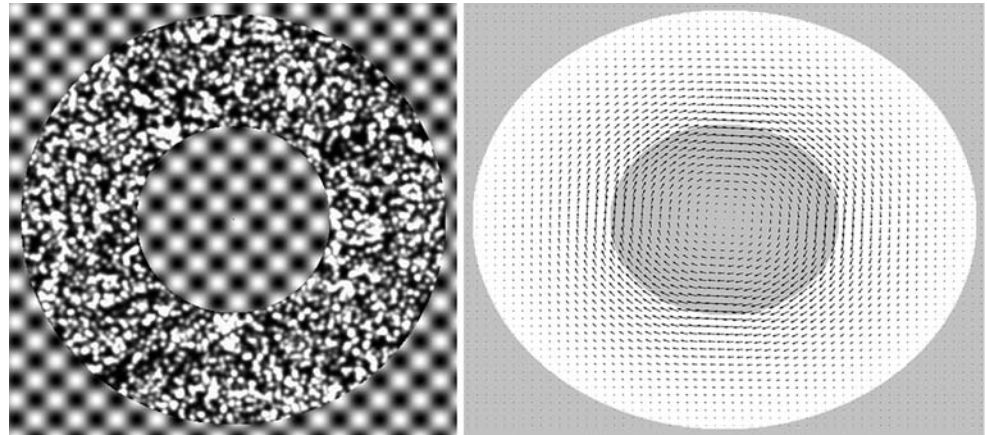


Fig. 9 From the visual impression, both velocity fields resemble the true motion extremely well. *Left:* Reconstructed velocity field (penalization everywhere) *Right:* Reconstructed velocity field (no penalization on boundary)

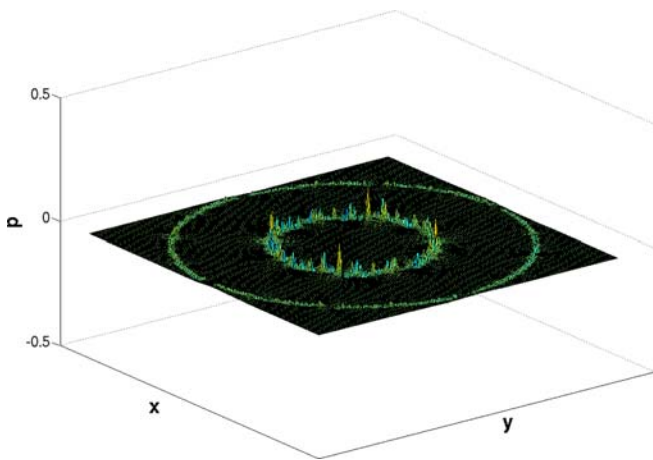
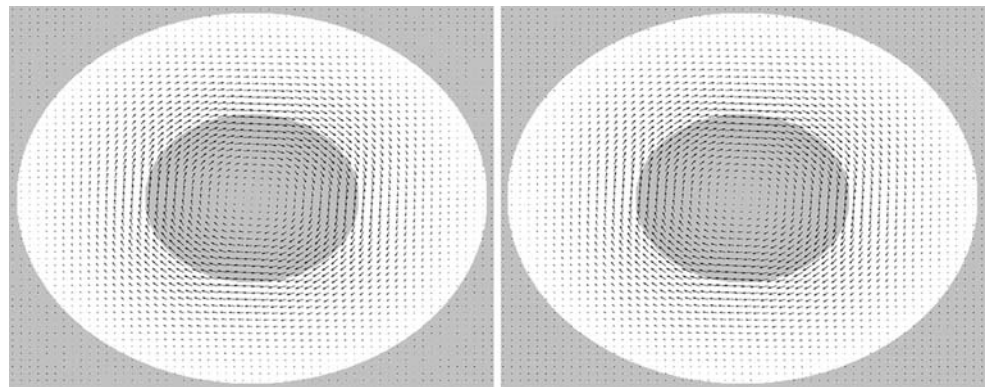
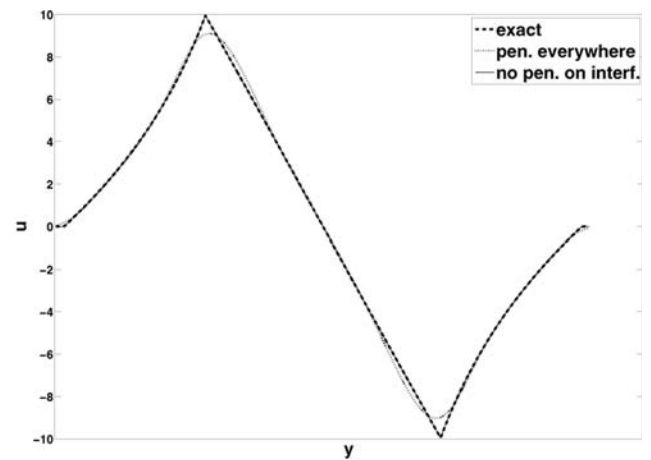


Fig. 10 *Left:* Reconstructed pressure distribution (no penalization on boundary): p is zero almost everywhere, some numerical instabilities at the interfaces. *Right:* Profile of the velocity



distribution. Note that, if we penalize everywhere, the reconstructed velocity field is much too smooth

intensity function was generated as in the preceding cases (Sect. 4.1). Its size is 256×256 pixels. The maximum displacement is approximately 3.5 pixels. We want to analyze this image pair using the following approaches:

- *Multi pass cross correlation* (LaVision 2005): Advanced cross-correlation approach (LaVision Davis 7.1.1.34). Initial interrogation window size 32×32 , final interrogation window size 8×8 and

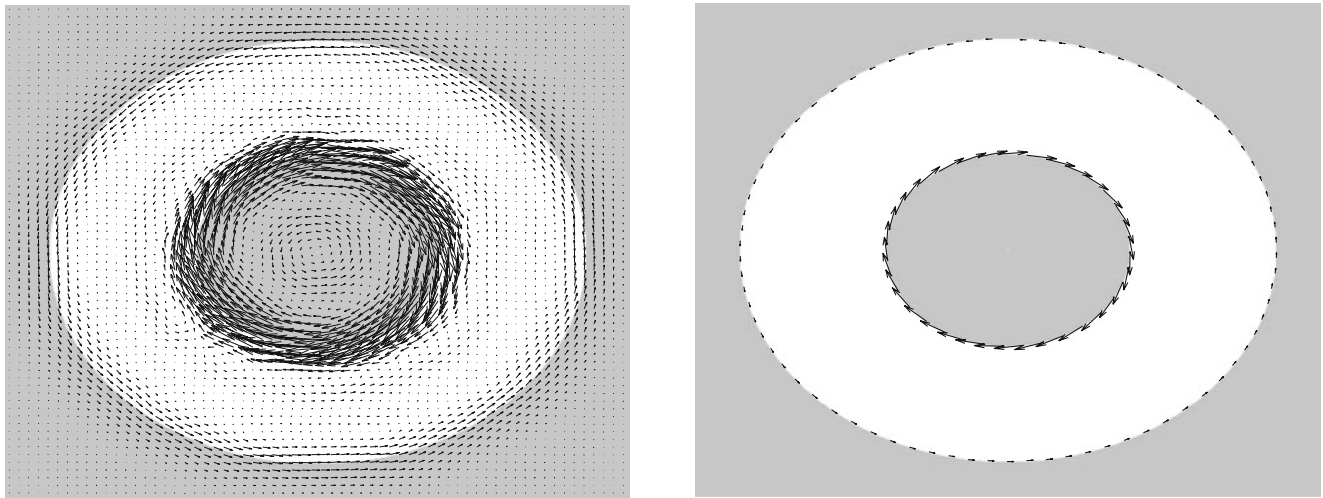


Fig. 11 Reconstructed body force. *Left:* Penalization everywhere (force scaled by 10,000). *Right:* No penalization on interfaces (force scaled by 100). The frictional forces at the cylinder interfaces are extracted correctly

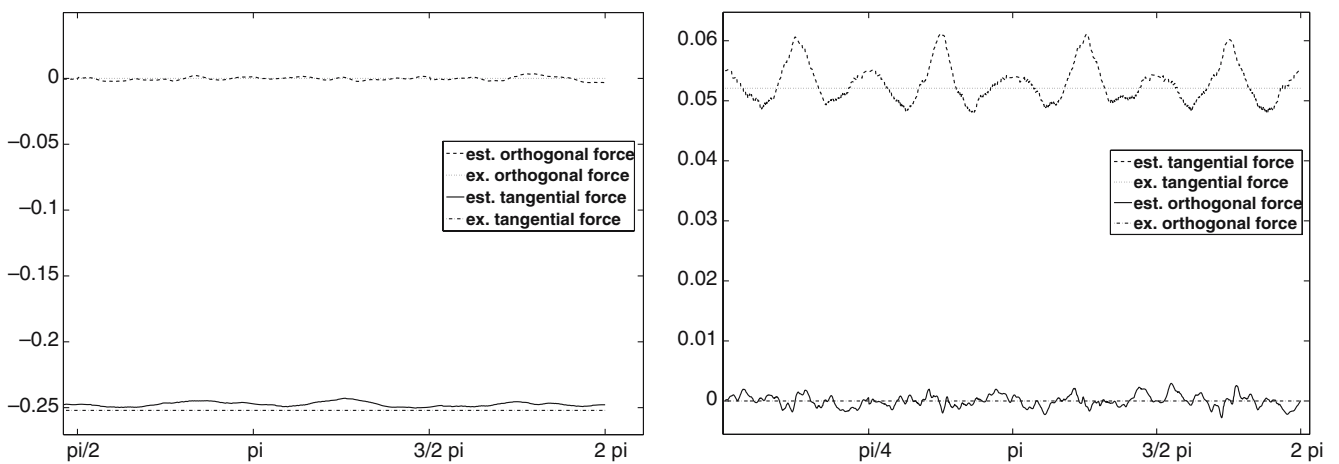


Fig. 12 Optical Stokes flow is able to compute the forces that act on the cylinder interfaces. *Left:* Tangential and orthogonal forces at the inner cylinder boundary. *Right:* Tangential and orthogonal forces at the outer cylinder boundary

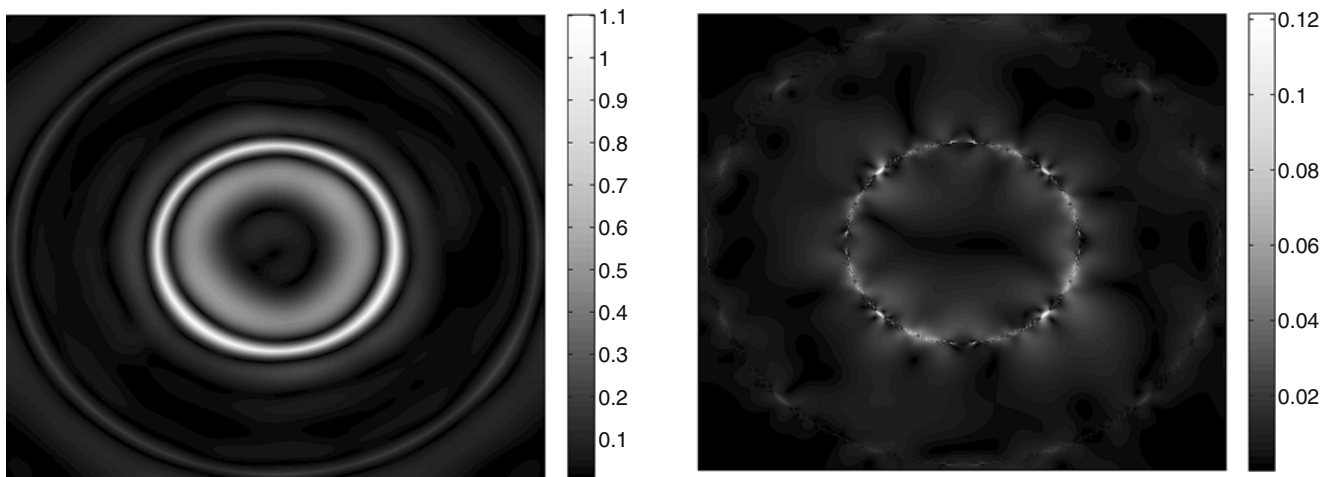


Fig. 13 *Left:* RMS velocity error (av. 0.110 pixel) when penalizing the body force everywhere. *Right:* RMS velocity error (av. 0.0079 pixel) when no penalization on the cylinder boundaries is performed

50% overlap manually selected for best performance. In order to interpolate the velocity vectors to the fine grid (i.e., one vector per pixel), second order spline interpolation is used.

- *Horn and Schunck* (Ruhnau et al. 2005): First-order regularization, no incompressibility constraint is imposed (cf. Eq. 5). The smoothness parameter $\lambda = 0.005$ was manually selected for best performance.
- *2nd order regularization* (Yuan et al. 2005): These authors use higher-order regularization (cf. Eq. 6) with an additional incompressibility constraint. Instead of mixed finite elements (as we do), the authors use the so-called mimetic finite differencing scheme. Temporal coherency is not exploited. Parameters: $\lambda_1 = 0.5$, $\lambda_2 = 0.05$, manually selected for best performance.
- *Optical Stokes flow computation (this paper)*: $\mu = 1$, $\alpha = 100$, $\gamma = 200$ selected by hand.

Figure 15 shows the spatial error distributions for the different algorithms. Note that all variational approaches are able to outperform the cross-correlation method. Optical Stokes Flow computation yields the best results (average RMS error = 0.0484 pixels). Figure 16 compares the vorticity estimates for the cross-correlation approach and optical Stokes flow estimation.

Figure 17 shows how well the individual approaches are capable of recovering the different frequencies of the vorticity. While the spectrum of the optical Stokes flow estimate resembles the true spectrum very well, cross-correlation seems to underestimate higher frequencies. This had to be expected since cross-correlation relies on the assumption that the velocity gradient within an interrogation window is negligible. Even advanced window deformation techniques cannot fully resolve the high frequencies that are present in the velocity field.

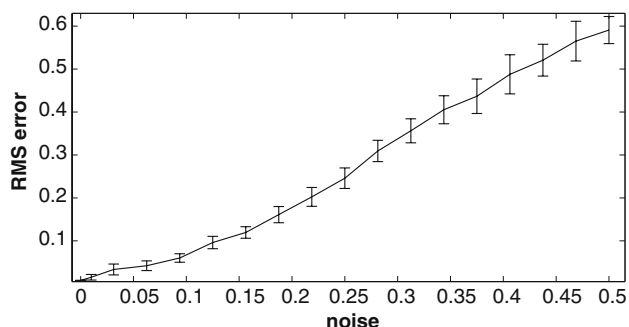


Fig. 14 RMS velocity error (in pixels) when adding different amounts of Gaussian noise (zero mean and variance up to 50%.)

It is interesting to note that optical Stokes flow gives extremely good results even though its prior knowledge is inadequate. In order to understand this fact, let us first summarize what type of prior knowledge the competing approaches use:

- The cross-correlation approach assumes that the velocity field is piecewise constant. This assumption is weakened by advanced window-deformation techniques.
- The Horn and Schunck method assumes small velocity gradients.
- Higher-order div curl regularization assumes a smooth vorticity.

This compilation shows that the priors of all analyzed approaches are severely inadequate. It is clear that we are currently at the starting point towards physically more and more plausible regularizers and that optical Stokes flow is the most plausible regularizer that is currently available. In the conclusions section we will state in which direction we expect research to go on.

4.2.2 Highly non-rigid real world image pair

Figure 18 shows a sample image of the experimental evaluation of the spreading of a low diffusivity dye in a 2D turbulent flow, forced at a large scale. In contrast to the preceding examples, no tracer particles were brought into the fluid but a mixture of fluorescein and water. For more details about the experimental setup, we refer to Jullien et al. (2001). Cross-correlation approaches are not able to extract valid velocity fields for this type of input data (passive scalar images). Figure 18 shows, however, that our optical Stokes flow approach is capable of extracting a very reasonable velocity distribution. We chose the same parameters as in Sect. 4.2.1.

4.2.3 Out-of-plane motion: separation bubble

The synthetic image sequence shown in Fig. 19 was generated by means of the software prescribed in Hain and Kähler (2005, 2005). Determination of the particle image displacements is based on the solution of a direct numerical simulation (DNS) of a laminar separation bubble.

The main problem in this example is the fact that the true velocity field of this sequence is three-dimensional (maximum out-of-plane velocity: 1 pixel⁵). Because we

⁵ We assume that the (imaginary) grid in out-of-plane direction has the same resolution as the in-plane grid.

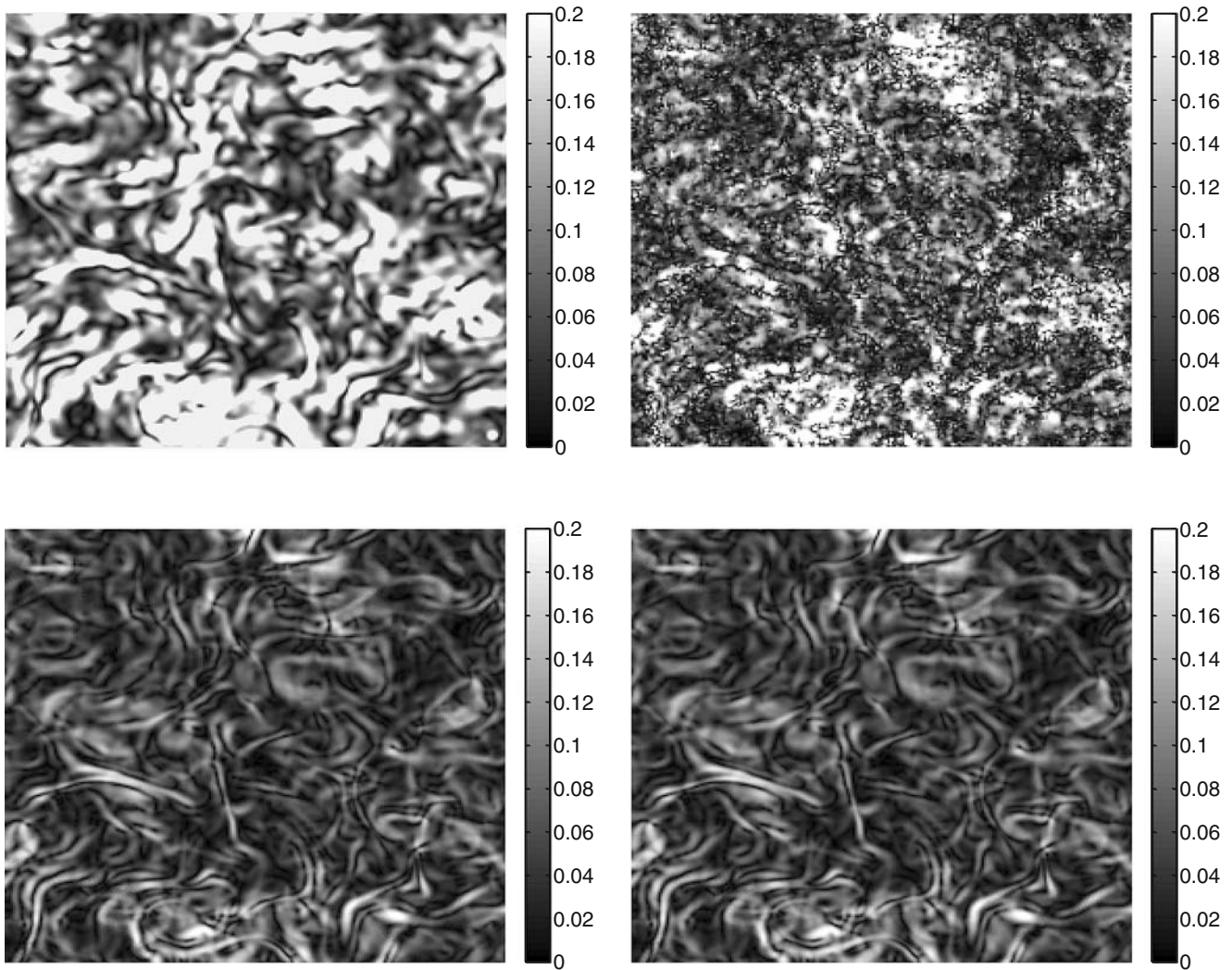
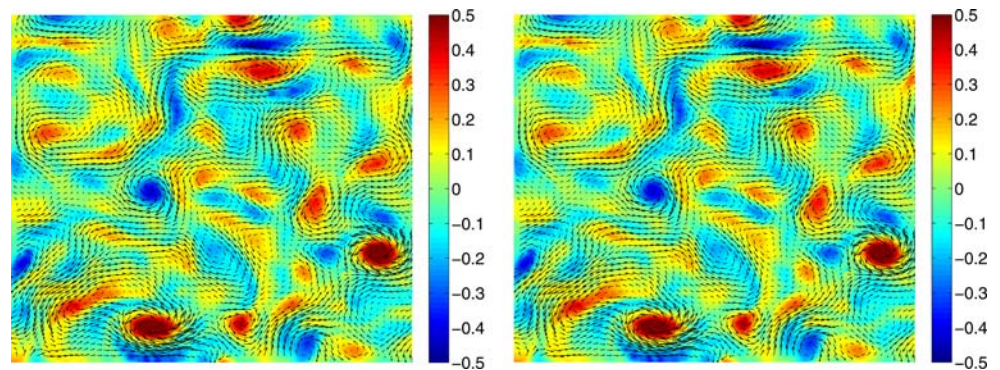


Fig. 15 *Top left:* Multi-pass cross-correlation (DaVis), av. err. = 0.1420 pixel. *Top right:* Horn and Schunck, av. err. = 0.0821 pixel. *Bottom left:* 2nd order regularization, av. err. = 0.0525 pixel. *Bottom right:* Optical Stokes flow computation, av. err. = 0.0484 pixel

Fig. 16 Estimated velocity field and its curl. *Left:* Cross correlation. *Right:* Optical Stokes flow. Note that cross-correlation slightly underestimates the vorticity



analyze a 2D projection, the divergence-free constraint, that is strictly enforced by the Stokes equation is not valid (cf. Fig. 21). This is why we use the modified method of Sect. 2.4 to analyze this image pair. Figure 20 compares the error of the cross-correlation

method with our modified Stokes equation’s velocity error. While cross-correlation yields an average error of 0.0331 pixel, the velocity field recovered by the modified Stokes approach is more reliable. Its average RMS error is 0.0212 pixels (Fig. 21).

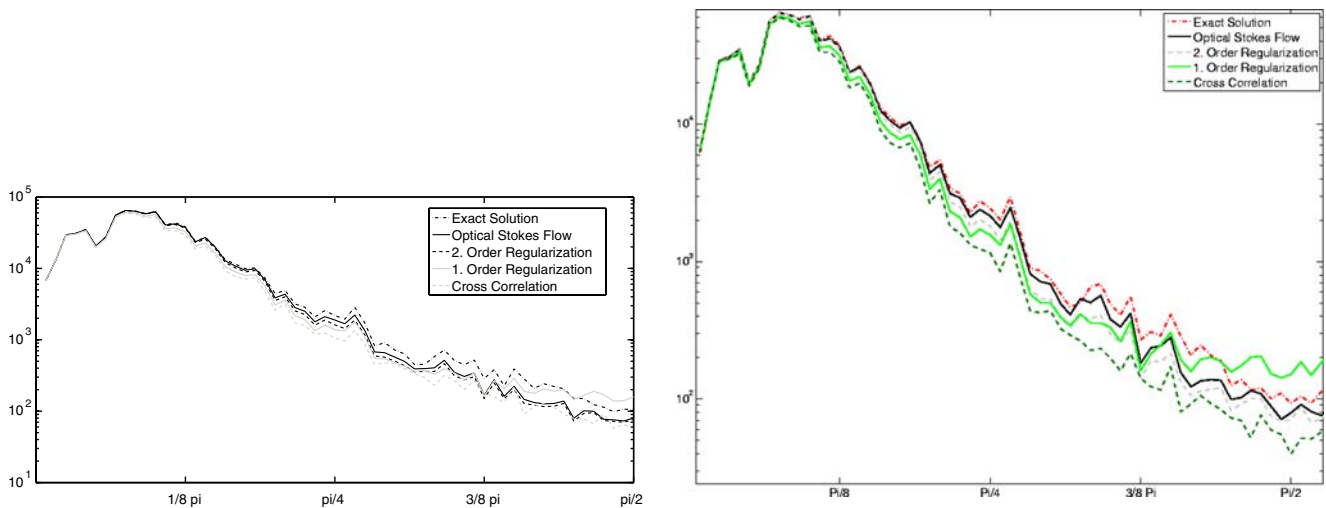


Fig. 17 Energy of the vorticity (for frequencies between 0 and $\Pi/2$) of the different algorithms (logarithmic plot). Energy spectrum of optical Stokes flow estimate is closest to the true solution, while cross-correlation underestimates higher frequencies

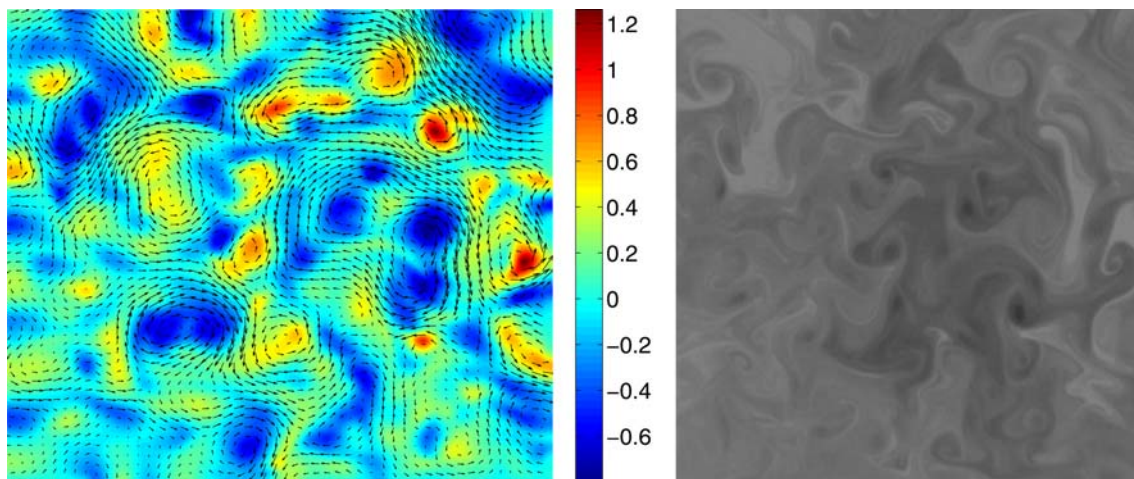
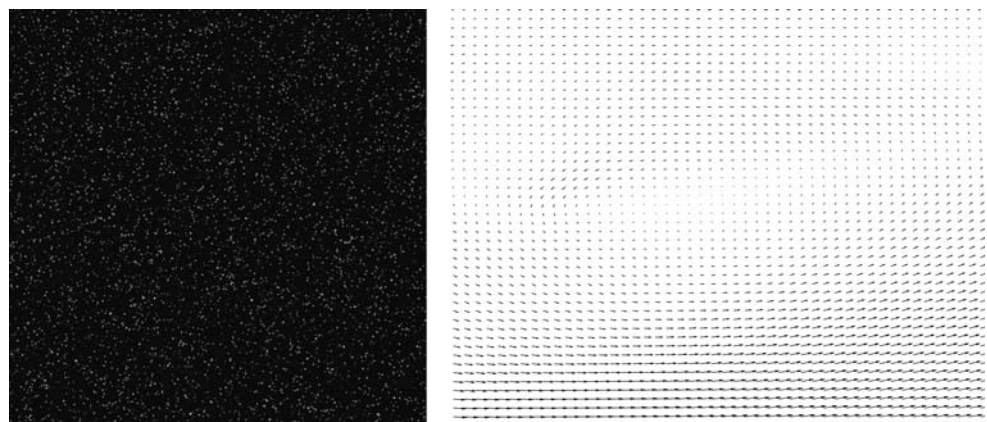


Fig. 18 *Left*: Passive scalar image (size: 512×512). *Right*: Recovered velocity field using optical Stokes flow ($\mu = 1$, $\alpha = 100$, $\gamma = 200$). Note that cross-correlation approaches completely fail for this type of image data

Fig. 19 *Left*: Synthetic image (separation bubble, size: 512×512). *Right*: Synthetic velocity field. Note that the velocity field is three dimensional. Therefore, particles leave and enter the illuminated image plane. Furthermore, the 2D projection is no longer divergence free



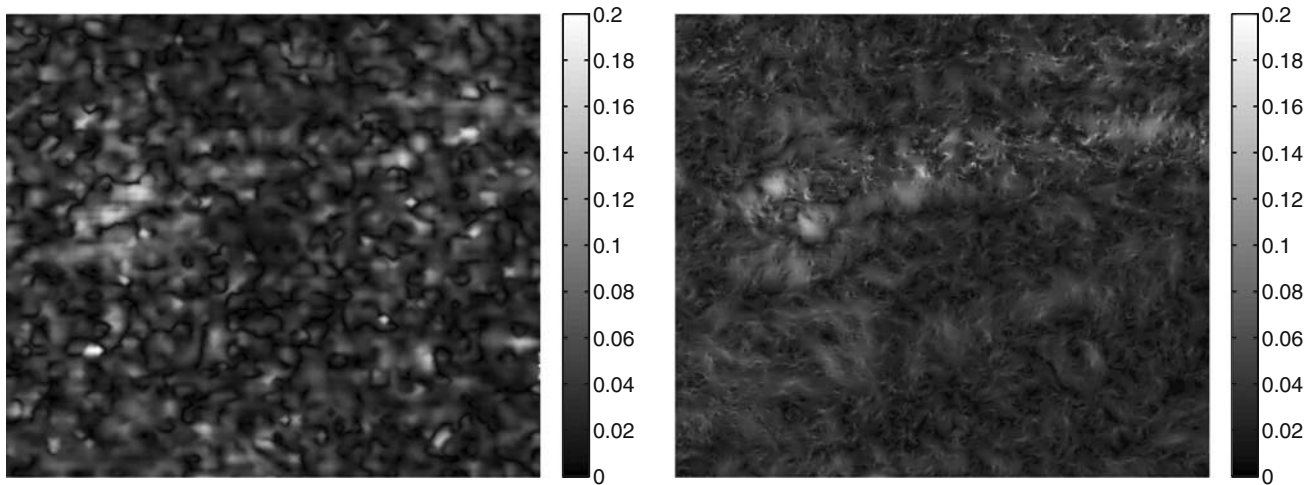


Fig. 20 *Left*: RMS velocity error of cross-correlation approach (smallest window size 16×16 , 50% overlap, mean RMS = 0.0331 pixel). *Right*: RMS velocity error of modified optical Stokes flow ($\mu = 1$, $\alpha = 100$, $\beta = 200$, mean RMS = 0.0212 pixel)

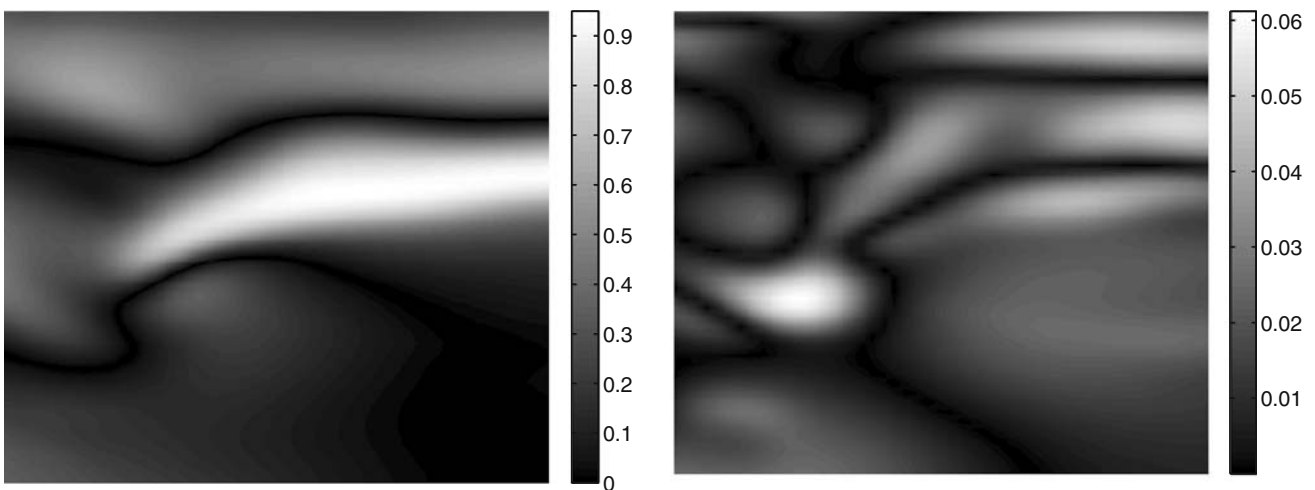


Fig. 21 Out-of-plane velocity (*left*) leads to divergence of the 2D projection (*right*). We have to use the modified optical Stokes flow approach to reliably reconstruct the target velocity field

5 Conclusions and further work

We presented a novel variational flow control approach for PIV that uses the Stokes equation as prior knowledge. Methods from distributed parameter control theory were used to solve the arising constrained optimization problem. The experimental evaluation showed that, as long as we confine ourselves to flows that are actually governed by the Stokes equation, the proposed algorithm is not only capable of reliably estimating the velocity fields between image pairs, but it can also extract the pressure distribution and forces acting on the fluid.

The experiments also showed that our approach is able to outperform other optical flow-based methods as

well as cross-correlation methods on highly non-rigid (Navier–Stokes) flows. The reason for this is the high resolution that can be achieved. We demonstrated that optical flow based approaches not only yield dense vector fields—with proper regularization that does not penalize velocity gradients—but that the spatial resolution of these fields compares favorably with cross-correlation approaches.

It has also been shown that a minor modification our approach without altering the overall computational structure (Sect. 2.4) enables the successful application of our approach also to scenarios where the out-of-plane velocity is not negligible.

Optical Stokes flow offers dramatic improvement when evaluating image pairs with dense gray value

functions (Fig. 18), whereas cross-correlation approaches completely fail. To summarize, the use of optical Stokes flow might be advantageous in the following three scenarios:

- Stokes flows: If the flow is actually governed by the Stokes equations, not only the velocity can be estimated but also pressure and forces that act on the fluid.
- Highly non-rigid flows: The increased spatial resolution that optical Stokes flow offers permits the estimation of high-resolution velocity fields.
- Scalar images: While cross-correlation approaches fail for this specific kind of image data, optical flow approaches give very reasonable velocity estimates.

Our future work will concentrate on two main aspects: first, in view of advanced measurement techniques (Elsinga et al. 2005), we will focus on three-dimensional flow analysis where imposing physical constraints is natural, and where other problems like out-of-plane motions will become obsolete. A second topic for future work is the extension of our approach to include the convection term of the Navier–Stokes equations, leading us to the study of involved nonlinear constrained optimization problems for estimating physically consistent fluid flows that may further increase the accuracy of image-based fluid flow estimation.

Acknowledgments The authors thank Johan Carlier (Cemagref) for providing the turbulent image pairs and Rainer Hain (TU Braunschweig) for providing the cross-correlation estimates. Support by the Deutsche Forschungsgemeinschaft (DFG, SCHN 457/6) within the priority programme “Bildgebende Messverfahren in der Strömungsmechanik” (www.spp1147.tu-berlin.de) and by the EU project “Fluid Image Analysis and Description” (<http://www.fluid.irisa.fr/>) is gratefully acknowledged.

References

- Braess D (1997) Finite elements. Theory, fast solver, and applications in solid mechanics. Springer, Berlin Heidelberg New York
- Brezzi F, Fortin M (1991) Mixed and hybrid finite element methods. Springer-Verlag New York, Inc., New York
- Carlier J, Heitz D (2005) 2D turbulence sequence provided by Cemagref within the European Project ‘Fluid Image Analysis and Description’. <http://fluid.irisa.fr/>
- Corpetti Th, Heitz D, Arroyo G, Mémin E, Santa-Cruz A (2005) Fluid experimental flow estimation based on an optical-flow scheme. *Exp Fluids* 40(1):80–97
- Elsinga GE, Scarano F, Wieneke B, van Oudheusden BW (2005) Tomographic particle image velocimetry. In: Proceedings of the 6th international symposium on particle image velocimetry (PIV’05), Pasadena, September 21–23
- Gunzburger M (2002) Perspectives in flow control and optimization. Society for Industrial and Applied Mathematics, Philadelphia
- Hackbusch W (1993) Iterative solution of large sparse systems of equations, vol 95 of Applied Mathematical Sciences. Springer, Berlin Heidelberg New York
- Hain R, Kähler CJ (2005) Advanced evaluation of time-resolved PIV image sequences. In: Proceedings of the 6th international symposium on particle image velocimetry, Pasadena, September 21–23
- Hain R, Kähler CJ (2005) Fundamentals in multiframe PIV. *Exp Fluids* (submitted)
- Horn B, Schunck B (1981) Determining optical flow. *Artif Intell* 17:185–203
- Jullien MC, Castiglione P, Tabeing P (2001) Intermittency of a passive tracer in the inverse energy cascade. *Phys Rev E* 64(3):035301
- Kaga A, Yamaguchi K, Kondo A, Inoue Y (1998) Combination of PIV data with cfd using cost function method. In: Proceedings of the 8th international symposium on flow visualization, p 257
- Kohlberger T, Mémin E, Schnörr C (2003) Variational dense motion estimation using the helmholtz decomposition. In: Griffin LD, Lillholm M (eds) Scale space methods in computer vision. LNCS, vol 2695. Springer, Berlin Heidelberg New York, pp 432–448
- Landau LD, Lifschitz EM (1952) Hydrodynamik. Number 6 in Lehrbuch der theoretischen Physik. Verlag Harri Deutsch, Thun, 5. (1991) edition
- LaVision (2005) DaVis. Software for Intelligent Imaging
- Lions JL (1971) Optimal control of systems governed by partial differential equations. Springer, Berlin Heidelberg New York
- Michaewicz Z (1994) Genetic algorithms + data structures = evolution programs. Springer, Berlin Heidelberg New York
- Nagel HH, Enkelmann W (1986) An investigation of smoothness constraints for the estimation of displacement vector fields from image sequences. *IEEE Trans Pattern Mach Intell* 8(5):565–593
- Nobach H, Ouellette NT, Bodenschatz E, Tropea C (2005) Full-field correlation-based image processing for PIV. In: Proceedings of the 6th international symposium on particle image velocimetry, Pasadena, September 21–23
- Nobach H, Tropea C (2005) Improvements to PIV image analysis by recognizing velocity gradients. *Exp Fluids* 39:614–622
- Ogawara K, Noborizato T, Iida S (1997) A moving least square PIV algorithm coupled with Navier–Stokes flow solver. In: Proceedings of the 2nd international Workshop on PIV’97
- Okamoto K, Nishio S, Kobayashi T (2000) Standard images for particle-image velocimetry. *Meas Sci Technol* 11:685–691
- Okuno T, Yasuhiko S, Nishio S (2000) Image measurement of flow field using physics-based dynamic model. *Meas Sci Technol* 11:667–676
- Ruhnau P, Gütter C, Schnörr C (2005a) A variational approach for particle tracking velocimetry. *Meas Sci Technol* 16(7):1449–1458
- Ruhnau P, Kohlberger T, Nobach H, Schnörr C (2005b) Variational optical flow estimation for particle image velocimetry. *Exp Fluids* 38:21–32
- Schnörr C (1991) Determining optical flow for irregular domains by minimizing quadratic functionals of a certain class. *Int J Comput Vis* 6(1):25–38
- Suter D (1994) Mixed-finite element based motion estimation. *Innov Tech Biol Med* 15(3):292–307
- Yuan J, Ruhnau P, Mémin E, Schnörr C (2005) Discrete orthogonal decomposition and variational fluid flow estimation. In: Proceedings of the 5th international conference on scale space and PDE methods in computer vision, vol 3459, pp 267–278